Twisted Crystalline Organic Semiconductor Photodetectors

Jeong, Sehee; Barbosa, Natercia; Tiwari, Akash; Holland, Emma K.; Huang, Ling-Yi; Bhat, Vinayak; Yang, Yongfan; Zhang, Yuze; Whittaker, St. John; Kim, Min-Woo; Alaei, Aida; Sundaram, Pallavi; Spencer, Rochelle; Brazard, Johanna [**and 7 more**]

How to cite

JEONG, Sehee et al. Twisted Crystalline Organic Semiconductor Photodetectors. In: Advanced functional materials, 2023, vol. 33, n° 19, p. 2212531. doi: 10.1002/adfm.202212531

This publication URL: https://archive-ouverte.unige.ch/unige:181113
Publication DOI: 10.1002/adfm.202212531

Twisted Crystalline Organic Semiconductor Photodetectors

Sehee Jeong,[a] Natercia Barbosa,[b] Akash Tiwari,[a] Emma K. Holland,[c] Ling-Yi Huang,[c] Vinayak Bhat,[c] Yongfan Yang,[a] Yuze Zhang,[d] St. John Whittaker,[a] Min-Woo Kim,[a] Aida Alaei,[a] Pallavi Sundaram,[a] Rochelle Spencer,[a] Johanna Brazard,[b] Dilhan Kalyon,[d] Chad Risko,[c] John E. Anthony,[c] Takuji B. M. Adachi,[b] Alexander G. Shtukenberg,[a] Bart Kahr,[a] and Stephanie S. Lee[,a]*

[a] Department of Chemistry and Molecular Design Institute, New York University, New York, New York, United States

[b] Department of Chemistry, University of Geneva, Geneva, Switzerland

[c] Department of Chemistry & Center for Applied Energy Research (CAER), University of Kentucky, Lexington, KY, United States

[d] Department of Chemical Engineering and Materials Science, Stevens Institute of Technology, Hoboken, NJ, United States

ABSTRACT

Optoelectronic properties of anisotropic crystals vary with direction requiring that the orientation of molecular organic semiconductor crystals are controlled in optoelectronic device active layers to achieve optimal performance. Here, a generalizable strategy to introduce periodic variations in the out-of-plane orientations of 5,11-bis(triisopropylsilylethynyl)anthradithiophene (TIPS ADT) crystals is presented. TIPS ADT crystallized from the melt in the presence of 16 wt % polyethylene (PE) forms banded spherulites of crystalline fibrils that twist in concert about

*Corresponding author. E-mail: stephlee@nyu.edu

This is the author manuscript accepted for publication and has undergone full peer review but has not been through the copyediting, typesetting, pagination and proofreading process, which may lead to differences between this version and the Version of Record. Please cite this article as doi: 10.1002/adfm.202212531.

the radial growth direction. These spherulites exhibit band-dependent light absorption, photoluminescence and Raman scattering depending on the local orientation of crystals. Mueller matrix imaging revealed strong circular extinction (CE), with TIPS ADT banded spherulites exhibiting domains of positive or negative CE signal depending on the crystal twisting sense. Furthermore, orientation-dependent enhancement in charge injection and extraction in films of twisted TIPS ADT crystals compared to films of straight crystals was visualized in local conductive atomic force microscopy maps. This enhancement led to photocurrents and external quantum efficiencies 3.3 and 6.2 times larger, respectively, in photodetectors comprising twisted crystals than those comprising straight crystals.

KEYWORDS: Organic semiconductor, banded spherulite, crystal anisotropy, crystal twisting, melt growth

1. INTRODUCTION

Crystal anisotropy can be friend or foe. Anisotropy can multiply material responses, but giving the vagaries of crystal growth, it may not be possible to access the most desirable direction. Controlling the orientation of highly anisotropic semiconductor crystals is therefore critical to the development of plastic electronics, in which the active layer is constrained in thin films. A promising single crystal may grow in a disappointing and unproductive direction when constrained in two dimensions.[1] It is possible however to grow films in a single crystallographic direction parallel to a substrate that presents multiple crystallographic directions in the perpendicular direction. This might seem like a contradiction, but we aim to illustrate a general strategy based on the growth guided twisting of crystals in thin films for simultaneously accessing multiple crystallographic directions at the same time.

Researchers have struggled to control particular orientations of semiconductors on substrates with the aim of aligning the π-stacking direction, typically the fastest direction for charge transport, in the substrate plane by shearing,[2] collimating growth in narrow channels[3] or applying temperature gradients.[4] Directing the π-stacking axis out of plane has been more challenging. Thermal evaporation of organic semiconductor materials for substrate modification can induce out-of-plane orientations.[5] Unencumbered aromatic moieties (pentacene, copper phthalocyanine) can lie parallel to the substrate, and thus naturally π-stack in the perpendicular direction.[5] Nano-confining scaffolds have been used to orient solution-processed crystals into vertical crystal arrays.[6] While much progress has been made in orientation

control, these methods optimize only a single direction for fast charge transport and their successful implementation depends on compound-specific properties, such as solubility and crystal growth habit.

Many fibrous crystals, under high driving forces, will twist as they grow.[7] This is a common morphological distortion in synthetic polymers; ca. 50% of high polymers can twist as they grow.[8] However, twisting is almost as common for crystals made from small organic molecules.[9, 10] It is estimated that approximately one-third of all organic molecules that melt can be induced to twist under some conditions, forming helicoidal fibrils as they grow.[9] Most commonly, the presence of highly viscous additives, such as naturally occurring resins or synthetic polymers, can promote small molecule crystal twisting. These additives can suppress nucleation to achieve higher degrees of undercooling and promote fibrillar crystal morphologies, both of which favor crystal twisting.[7] An even higher percentage of binary charge transfer complexes (23 out of 41 tested) can also form twisted morphologies.[11] Single twisted crystals can grow from solution or the vapor phase as well.[12] Melt crystallization often leads to radial aggregates growing from a common nucleation center as so-called optically banded spherulites. Rhythmic optical contrast arises when fibrils twist in concert about the growth direction, thus modulating the optical properties of the object. The pitch or the distance required for a 180° rotation typically range from microns to millimeters. Because of smooth rotations of crystal structures about direction parallel to the substrate, the crystallographic orientation normal to the substrate varies smoothly. Consequently, the anisotropic electronic and optical properties associated with the different orientations are thus modulated in films on this length scale.

We recently reported the effect of twisting on charge transport in binary charge transfer complexes (CTCs) comprising pairs of organic electron donors and acceptors.[11] The electron and hole mobilities for twisted pyrene-tetracyanoethylene (TCNE) (PyT) and phenanthrene-TCNE (PhT) polycrystalline thin-film transistors (TFTs) were three and four times higher than those of TFTs comprising straight crystals, respectively.[11] A monocomponent semiconductor, 2,5-bis(3-dodecyl-2-thienyl)-thiazolo[5,4-d]thiazole (BDT) shows improved charge mobilities for TFTs comprising twisted crystal active layers compared to straight crystal active layers, and mobilities vary inversely with pitch.[13] While large gaps were present between straight crystals, twisting promoted the formation of more frequent but smaller gaps, resulting in better film connectivity for charge transport. Modest improvements in mobility were also observed for TFTs comprising twisted tetrathiafulvalene (TTF) crystals compared to those comprising straight TTF crystals.[14] Helicoidal twisting breaks the centrosymmetry of TTF crystals on the mesoscale, leading to the differential interaction with left- or right-circularly polarized light (CPL) depending on the twist sense.

Herein, we report the spontaneous twisting of 5,11-bis(triisopropylsilylethynyl)anthradithiophene (TIPS ADT) crystals grown from the melt and investigate their optoelectronic properties. Compared to TTF[14] and the CTCs[11] studied thus far, TIPS ADT is superior at transporting charge and has a broader light absorption. Melt-processed TIPS ADT crystals were found to adopt a previously unreported high-temperature polymorph with a predicted brickwork packing motif via x-ray diffraction (XRD) analysis and density functional theory (DFT) simulations. When crystallized in the presence of 15-20 wt% PE, TIPS ADT forms banded spherulites, with absorption, photoluminescence and Raman spectra exhibiting band-dependent (crystal orientation-dependent) properties. The symmetry breaking arising from the helicoidal morphologies also led to unexpected optical properties that could not be predicted from the space group symmetry alone. The introduction of continuously rotating crystal orientations to TIPS ADT films of twisted crystals rendered films more conductive than those comprising straight crystals, resulting in enhanced photocurrent generation in TIPS ADT twisted crystal active layers. These observations suggest that crystal twisting may be a generalizable strategy to improve the performance of organic electronic devices.

2. RESULTS AND DISCUSSION

1–2 μm thick films of straight and twisted TIPS ADT crystals were grown by melting 1–2 mg of pure TIPS ADT and TIPS ADT mixed with medium density PE in a 5:1 ratio, respectively (16 wt% polymer), between two glass cover slips at 250 ºC. In this study, PE was chosen as a twisting additive because it readily forms banded spherulites on its own[15] and its T_m of 110 ºC is below that of TIPS ADT. Furthermore, PE, an insulating polymer, is electronically and optically distinct from TIPS ADT, so the role of twisting on electrical conductivity and interactions with visible light can be solely attributed to TIPS ADT. The samples were immediately cooled to a crystallization temperature, T_c, between 30 and 130 ºC on a Kofler bench. The samples were held at T_c until the films completely crystallized (within ten seconds) and subsequently further cooled to room temperature. Figure 1A and B display polarized light optical micrographs (POMs) of TIPS ADT spherulites crystallized from the melt at T_c = 130 and 30 ºC, without and with PE, respectively. For both films, crystallization was spherulitic with radial fibers growing from common centers.[7, 9] In the presence of PE, TIPS ADT spherulites showed concentric light and dark bands between crossed polarizers, a telltale sign of crystal twisting and a modulation of the linear birefringence (LB) and linear dichroism (LD) (Figure 1B).[16] The spacing between two bands of the same optical intensity, or the twisting pitch, P, was about 15–20 μm. PE acts as a

twist-inducing additive for TIPS ADT crystals but PE itself forms banded spherulites when crystallized from the melt below its melting temperature of ~110 ºC, albeit with much larger nucleation densities and smaller *P* values compared to TIPS ADT/PE blends crystallized at the same temperature (Figure S1).[17] Hereafter, we refer to TIPS ADT films comprising straight and twisted crystals as *S* and *T* films, respectively.

Figure 1C and D display 2D grazing-incidence X-ray diffraction (GIXD) patterns of *S* and *T* films, respectively. Strong diffraction peaks indicated high degrees of crystallinity. The peak locations were the same between samples, except for a small peak at q = 1.53 Å^{-1} corresponding to crystalline PE in the diffraction pattern collected on twisted TIPS ADT crystals (the only sample with PE). 1D line scans along q_{xy} = 0 Å^{-1} extracted from the diffraction patterns in Figure 1C and D compare poorly to the published single crystal structure of TIPS ADT (Figure 1E),[18] which adopts the so-called slip-stack (SS) packing motif.

The crystal structure of this new TIPS ADT polymorph was evaluated based on high-resolution powder X-ray diffraction data collected at the Advanced Photon Source at Argonne National Laboratory (Figure S2). The lattice constants were determined with the indexing software McMaille v3.04[19] and refined using Pawley fit implemented in Bruker TOPAS 6 software[20] with R_{wp} = 11.3%. The unit cell dimensions determined at 100 K were a = 7.527 Å, b = 7.86 Å, c = 16.576 Å, α = 78.44°, β = 89.914°, γ = 77.249°, V = 936.083 Å^3, Z = 1. The crystal structure was solved in the $P\bar{1}$ space group by the simulated annealing procedure implemented in TOPAS 6. A rigid aromatic body was constructed based on a TIPS ADT molecule from the experimental SS polymorph (CSD refcode FANGUX) with silyl and all isopropyl groups able to rotate freely. The final refinement provided R_p = 18.7% R_{wp} = 23.8% R_{exp} = 4.5%, gof = 5.24 (Figure S2A, CCDC-2213185). The flipped orientation of anthradithiophene core was introduced and its occupancy was refined to 13%. Relatively high values of *R*-factors are likely related to orientational disorder in silyl groups, which was found for the experimental SS polymorph (CSD refcode FANGUX). The presence of disorder in the crystal structure manifests itself by variations in half-widths of reflections with similar 2θ positions. The crystal structure was further validated by optimization using density functional theory (DFT; see Experimental Methods) with the same unit cell dimensions in the space group *P*1, which led to small changes in the molecular geometry and orientation and R_{wp} = 26.7 % (Figure S2B, Table S1). This crystal structure exhibits a brickwork (BW) packing motif, similar to that adopted by both 6,13-bis(triisopropylsilylethynyl)pentacene (TIPS PEN, d_{001} = 15.4 Å)[21] and 5,11-bis(triethylsilylethynyl)anthradithiophene (TES ADT, d_{001} = 16.9 Å) crystals.[22, 23]

Based on the BW motif, the diffraction peak at q = 0.4 Å^{-1} corresponds to the 001 reflection. The intensity of this reflection in the diffraction pattern collected on a *S* film is strongest along q_{xy} = 0 Å^{-1}, indicating that straight crystals preferentially orient with the (001) plane parallel to the substrate. In this orientation, the π-stacking direction is parallel to the substrate, as are sheets of the insulating silyl groups. This orientation, consistent with that observed for solution-processed crystals of TIPS PEN,[24] TES ADT[23] and other similar compounds,[25] is driven by favorable interactions between the bulky silyl groups and the underlying substrate. The 010 reflection appears most intense at q_z = 0 Å^{-1}, consistent with straight fibers growing along [010] corresponding to the π-stacking direction along which fastest growth occurs (Figure 1F). Twisted fibrils in *T* films also grow along the [010] direction but the plane parallel to the substrate surface alternates between the (001) and (100) planes as the crystals twist about the growth direction.

TIPS ADT spherulites grown from the melt with 16 wt% PE at T_c ranging from 30 to 130 ºC are shown in Figure 2A – D between crossed polarizers. All films crystallize as banded spherulites with concentric rings. *P* decreased with decreasing T_c (Figure 2E), that is the twisting frequency increased. At T_c below 100 ºC, P = 15 ± 5 μm, with circular bands indicating in-phase twisting of individual crystallites. At T_c = 110 and 130 ºC, *P* increased to 60 ± 30 μm and 170 ± 40 μm, respectively, however, the band edges become irregular. The crystallization driving force increases with decreasing crystallization temperature, which increases the aspect ratio of fibrils that twist more compared to thicker counterparts. Decreasing T_c thus results in smaller *P* values.[26] The same trend has been observed for many polymers, such as poly(3-hydroxybutyrate),[27] poly(vinylidene fluoride)[28] and poly(ethyleneterephthalate),[29] and numerous small molecules, including mannitol,[30] coumarin,[31] resorcinol,[32] tetraphenyl lead,[10] and BDT.[13]

POMs of PE after selective TIPS ADT removal by immersion in acetone (the red films become colorless) in Figure 2F – I reveal that the PE phase is left behind in banded spherulites with the same *P* as the TIPS ADT/PE composite. These results demonstrate that crystalline TIPS ADT and PE phases twist in concert with one another both above and below the PE melting point of 110 – 115 ºC. We expect molten PE to phase separate into the gaps between TIPS ADT twisted crystals as they grow radially outwards from the spherulite center. For samples in which T_c = 110–130 ºC, PE likely crystallizes after the samples cool to room temperature. Even though PE twists in the absence of TIPS ADT with its own characteristic pitch,[17] here the pitch seems to be determined by a templating effect of the more abundant host.

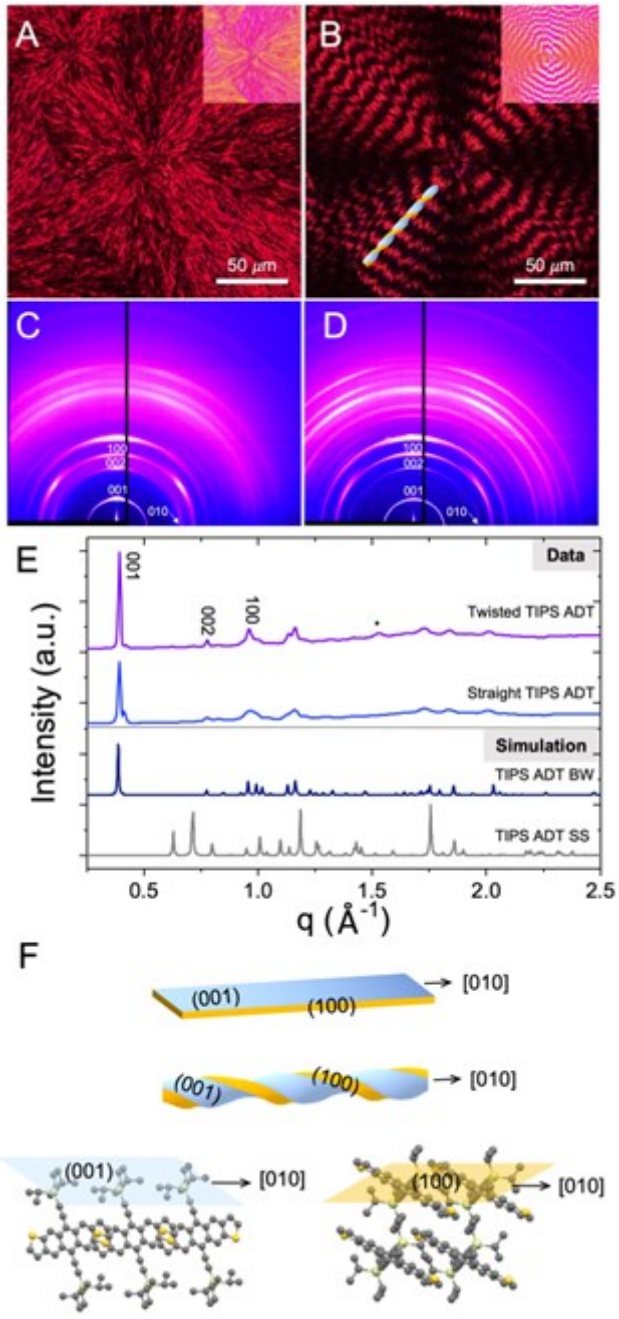

Figure 1. Polarized light optical micrographs and corresponding two-dimensional GIXD patterns of films comprising (A, C) straight TIPS ADT crystals (*S* film) grown from the melt at T_c = 130 ºC and (B, D) twisted TIPS ADT crystals (*T* film) grown from the melt at 30 ºC in the presence of 16 wt% of PE. Inset: Optical micrographs of the films in linearly polarized light. (E) 1D line scans extracted from the 2D diffraction patterns along q_{xy} = 0 Å^{-1}. Simulated powder diffraction patterns of the experimentally determined TIPS ADT crystal structure with a slipstack (SS) packing motif and the DFT-optimized crystal structure with a brickwork (BW) packing motif are provided for comparison. (F) Schematic illustrations of a straight and twisted fibril, highlighting (001) and (100) planes in blue and orange, respectively. Molecular orientations relative to these planes are also provided.

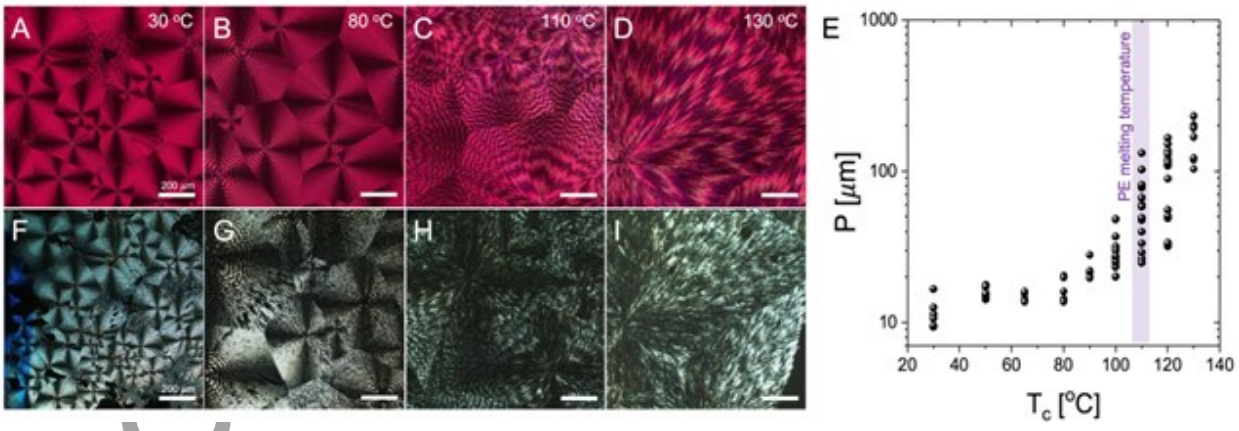

Figure 2. POMs of *T* films crystallized at (A) T_c = 30 °C, (B) T_c = 80 °C, (C) T_c = 110 °C, and (D) T_c = 130 °C, respectively. (E) Twisting pitch, *P*, versus T_c for *T* films. (F-I) POMs of remaining PE films after selective dissolution of TIPS ADT corresponding to (A-D), respectively.

Figure 3A displays cross-sectional scanning electron micrographs (SEMs) perpendicular to the spherulite fast growth direction both before and after selective TIPS ADT removal from TIPS ADT/PE films crystallized at T_c = 30 °C. In the top image, crystalline fibrils growing in and out of the plane of view are clearly observed. The fibrils alternate between vertical and horizontal orientations with respect to the substrate surface. In some cases, bending of the fibrils near the glass interfaces is observed. The remaining PE after TIPS ADT removal is highly porous, with fibrils adopting the same orientations as observed in the cross-section of the TIPS ADT/PE film. Figure 3B displays cross-sections *parallel* to the spherulite growth direction. In this case, fibril twisting is clear, with orientations alternating between edge-on and flat-on. While other semiconducting small-molecule/insulating polymer blends have exhibited vertical phase separation when cast from solution as thin films,[33] SEM images demonstrate that TIPS ADT and PE are intimately mixed throughout the film depth, forming domains on the sub-micron length scale that twist in concert with one another.

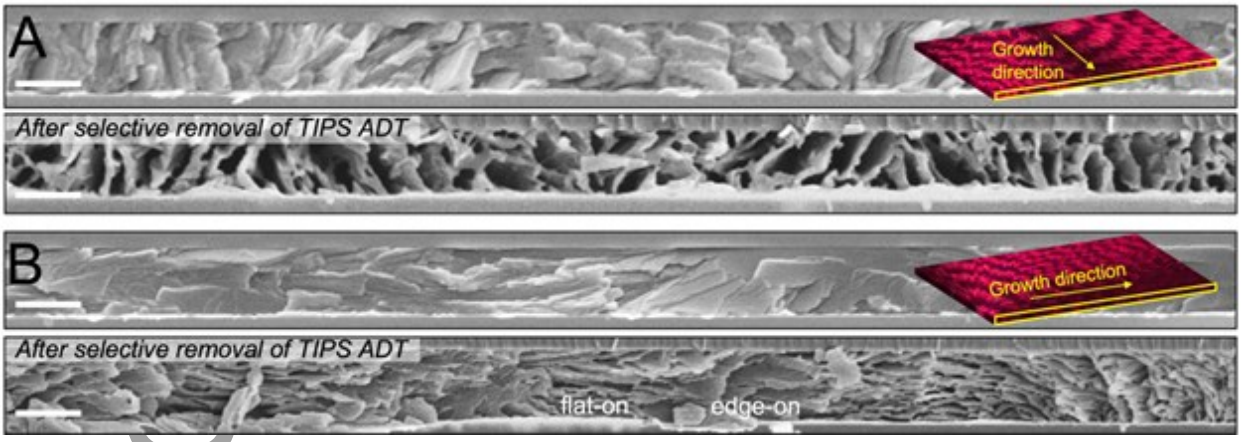

Figure 3. Cross-sectional SEMs of a twisted TIPS ADT film (*T* film) crystallized from the melt at T_c = 30 ºC collected (A) perpendicular and (B) parallel to the spherulite growth direction, as indicated by the inset illustrations. For both orientations, SEMs were collected before (top) and after (bottom) selective TIPS ADT removal. Scale bars = 1 μm.

Continuous rotation of TIPS ADT fibrils about the growth direction results in rhythmic oscillations in optical properties, including in refractive indices as observed in the POM in Figure 1B and PL intensities as observed in confocal fluorescence micrographs (Figure S3). Local absorption and PL spectra of light and dark bands of *T* film and those of the *S* film were collected using a microscope equipped with a microspectrophotometer with an aperture size of 5 μm (see Figure S4 for corresponding POM images). The thickness of *S* and *T* films we investigated here are about 1 μm. The polarization angle-dependent absorption spectra of dark and light bands of a *T* film (Figure 4B and C, respectively) exhibit peaks at 577, 540, 503 and 427 nm, labeled 1, 2, 3, and 4, respectively, the same as those observed in *S* film (Figure 4A) and similar to those of related acenes.[18, 34, 35] In all cases, the absorption spectra of melt-processed TIPS ADT films were red-shifted compared to that of both solution and solution-processed TIPS ADT films adopting the SS packing motif (Figure S5). This shift is attributed to increased π-orbital overlap between adjacent molecules in the BW packing motif.[35] Direct band gaps for BW and SS packing motifs using the GW-Bethe-Salpeter equation (BSE) were calculated to be 2.5 and 2.8 eV, respectively (Figure S6). Correspondingly, the lowest-energy singlet exciton peak (denoted by E_{S1}) in the GW-BSE-determined absorption spectra is blue-shifted for SS packing compared to BW packing (E_{S1} = 514 nm in SS packing, while E_{S1} = 593 nm in BW packing), as displayed in Figure S7A. Though GW-BSE has been known to produce errors in the absorption spectra of some systems, in both peak position and intensity, mostly due to the Tamm-Dancoff approximation,[36] it is still the most accurate method to date to predict the optical gap (E_{S1}) of an organic semiconductor with typical error about 0.1 eV.[37] Comparing the optical gaps of three curves in Figure S7A, we confirm that the TIPS ADT polymorph formed from the melt adopts the BW packing motif (the errors for the

first/lowest two peaks are within 0.06 eV), not SS (E_{S1} in SS packing is 0.26 eV higher than that of the experimental spectrum).

Non-negative matrix factorization (NMF), an unsupervised principal component analysis method,[38] was applied to each set of polarization angle-dependent absorption spectra collected on a *S* film and the bands that appear dark and light when viewed between crossed polarizers (see Figure S4B and S4C for corresponding POM images) for a *T* film to deconvolve each spectrum into a weighted sum of individual base spectra. The number of base spectra, the only pre-determined parameter in this analysis, was set to two. Figures 4D – F display the base spectra and their relative amplitudes as a function of polarization angle, with 0° corresponding to the direction parallel to the [010] fast growth direction. Comparisons of the NMF-generated and experimental spectra are provided in Figure S8 – S10. For *S* films, Peaks 2 – 4 are more intense in Base Spectrum 1, while Peak 1 is more intense in Base Spectrum 2. The relative amplitude of Base Spectrum 2 decreased from 100 to 0% with increasing polarization angle from 0 to 90°, indicating that the lowest energy transition associated with Peak 1 is strongly coupled to light polarized along the direction of overlapping anthradithiophene cores along the *b* direction, characteristic of a band with appreciable charge-transfer character (purple arrow in Figure 4G). Similar polarization angle dependence of the lowest energy peak was previously observed for TIPS pentacene and triethylsilylethynyl (TES) pentacene.[39] For TIPS pentacene, this peak was assigned to the first singlet excited state (S_1) and exhibited maximum intensity when the light polarization direction aligned with the direction of maximum overlap between the molecular short axis.[40] The relative amplitude of Base Spectrum 1 follows the opposite trend, increasing from 0 to 100% with increasing polarization angle from 0 to 90°. The transitions associated with Peaks 2 – 4 are thus likely related to excited states whose transition dipole moments are aligned with the long axis of the anthradithiophene core.

As displayed in Figure 4E, the NMF-determined base spectra and relative amplitudes extracted from the polarization angle-dependent absorption spectra of a dark band in a *T* film closely matches those of the *S* film. For the light band of a *T* film, on the other hand, the NMF-determined base spectra and weights are different. In particular, the intensity of Peak 1 is the same in both base spectra and thus does not display a polarization dependence (Figure 4F). This analysis suggests that the crystal orientation in the center of the dark band is the same as that in *S* films, i.e. with the (001) plane parallel to the substrate surface, while crystals are oriented with the (100) plane parallel in the center of the light band. Simulated absorption spectra (Figure S7B) also exhibit crystal orientation dependence, with the low energy absorption peak exhibiting a stronger intensity in the *ab* plane compared to the *bc* plane. Band-dependent Raman

spectra collected with a 785 nm depolarized laser and a spot size of 1 μm also confirm that the molecular orientation in the dark bands of *T* films is more like that in *S* films compared to light bands (Figure S11–13).

Mueller matrix imaging (MMI) was used to quantitatively map linear extinction (LE) and circular extinction (CE). The instrument was built from an inverted light microscope customized with dual mechanically rotating quarter wave plates as polarization modulators.[14, 30] The recorded intensities at each pixel for every combination of states for a polarization generator and a polarization analyzer are then used to evaluate the Mueller matrix, **M**, given by the following equation: $\mathbf{S_0} = \mathbf{MS_i}$, where $\mathbf{S_i}$ is the Stokes vector representing the polarization state of incoming light and $\mathbf{S_0}$ is that of exiting light.[41] LE, CE, are encoded in the 16-element matrix, **M**, which relates input polarization states to output polarization states. We use LE and CE in place of linear dichroism (LD) and circular dichroism (CD) because films with twisted fibers are not homogeneous along the light path and the dissipative optical effects do not have a singular interpretation. Figure 5A and C display the LE micrographs of *S* and *T* films, respectively. The LE signal of the *S* film is fairly uniform across the spherulites but exhibits some heterogeneity resulting from the presence of a non-zero distribution of out-of-plane crystal orientations. For the *T* film, on the other hand, the LE signal exhibits regular oscillations along the radial direction from the spherulite center commensurate with the twisting pitch, *P*.[42] This modulation in LE is in part the result of the continuous rotation of crystallographic orientations about the spherulitic growth direction, with different crystal orientations in a material with anisotropic extinction coefficients depending on the orientation-dependent polarizability of TIPS ADT molecules with respect to the direction of incoming light.

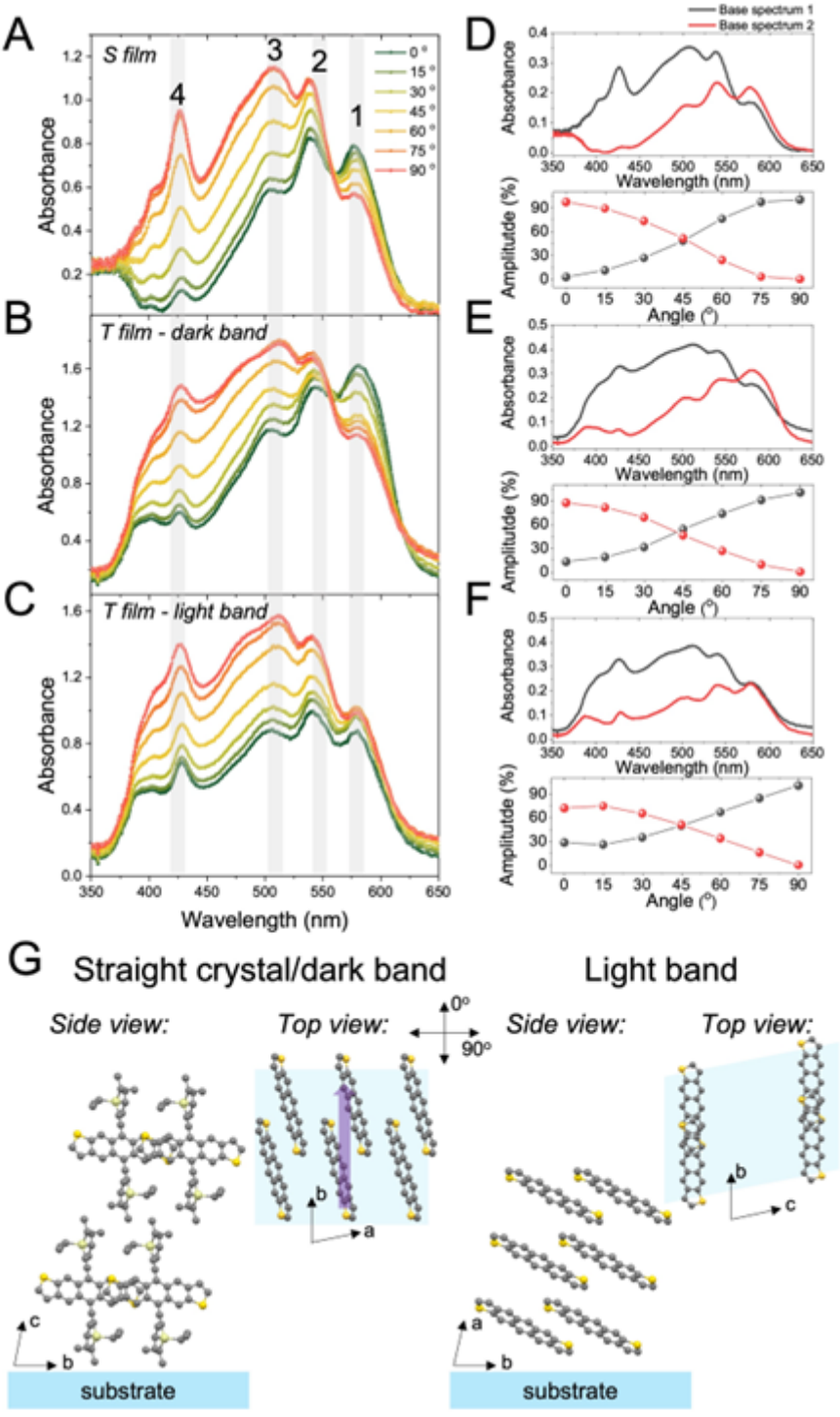

Figure 4. (A) Polarization angle-dependent absorption spectra collected on (A) a *S* film, (B) dark and (C) light bands of a *T* film using an aperture size of 5 μm. (D) – (F) Base spectra and their relative amplitudes as a function of polarization angle extracted from NMF analysis of the absorption spectra in (A) – (C). (G) Illustrations of molecular orientations in light and dark bands from side and top views. Purple arrow indicates direction of maximum π-orbital overlap, which is parallel to the *b* axis. Silyl groups have been removed from the top views and side view of the light band for clarity.

No systematic CE signal was observed for *S* films. This is to be expected for a $P\bar{1}$ crystal structure that does not admit natural optical activity. On the other hand, the corresponding image of a *T* film shows that each spherulite is bisected into domains, one with a positive CE signal and another with a negative signal. This signal is too strong to be a consequence of natural optical activity. It has been previously observed for centrosymmetric crystals that enantiopolar faces become unstable and nucleate crystallites that twist in opposite directions depending on the sense of the faces from which they arise. This heterochiral twisting, coupled with splaying of helicoidal lamellae to fill the space of the spherulite, can create heterogeneities along the light path that mimic circular birefringence (CB) or circular dichroism (CD) arising from the stacking anisotropic lamellae with a systematic sense of offset. Such optical activity associated with the film morphology, as opposed to the molecular or crystal structure, is a common feature of banded spherulites[43] and has been observed in melt-processed films of phthalic acid,[44] aspirin,[45] charge transfer complexes,[11] tetrathiafulvalene,[14] and BDT,[13] among others. One possibility for the signal in Figure 5D – F could be the coupling of linear birefringence (LB) and linear dichroism (LD), in particular a term of the form 1/2 (LD′·LB − LD·LB′) where the primes indicate birefringence and dichroism measured at a second of orthogonal axes at 45° with respect to the principal axes of the experiment. This coupling has the effect of producing a signal in a CD spectropolarimeter.[46]

As our films are both anisotropic and dichroic, there is a good reason to suspect that the origin of our CE signal in Figure 5D – F may arise in linear anisotropies and heterogeneities along *z*. A test for this effect is to reverse the wave vector, or more conveniently to flip the sample over. Unlike natural CD which is independent of the sign of the wave vector, $\pm k$, 2 (LD′·LB − LD·LB′) will change sign if interrogated from the opposite direction. As seen in Figure 5D and F that show the sample and the sample flipped about a horizontal axis, the signal does not change sign and therefore it does not arise from this second order effect. The sign of the CE signal is however dependent upon the wavelength. This may be a consequence of the change in the sign of the underlying LD as the dominant electronic state changes with frequency. The coupling of misoriented layers with LD can give rise to CD in the same way that misoriented layers with LB can give rise to CB.[43] Alternatively, the differential circular scattering related to Fresnel reflection dichroism at twisted interfaces can also give rise to differential circular scattering and thus CE. This has been observed in the visible spectrum in samples that were fully transparent.[44] A full accounting of the linear optical properties of these complex absorbing, heterogeneous, mesotextured, anisotropic films is the subject of an independent study that will require a fuller assignment of the electronic transitions and their polarizations of the new polymorph of TIPS ADT than we have at present.

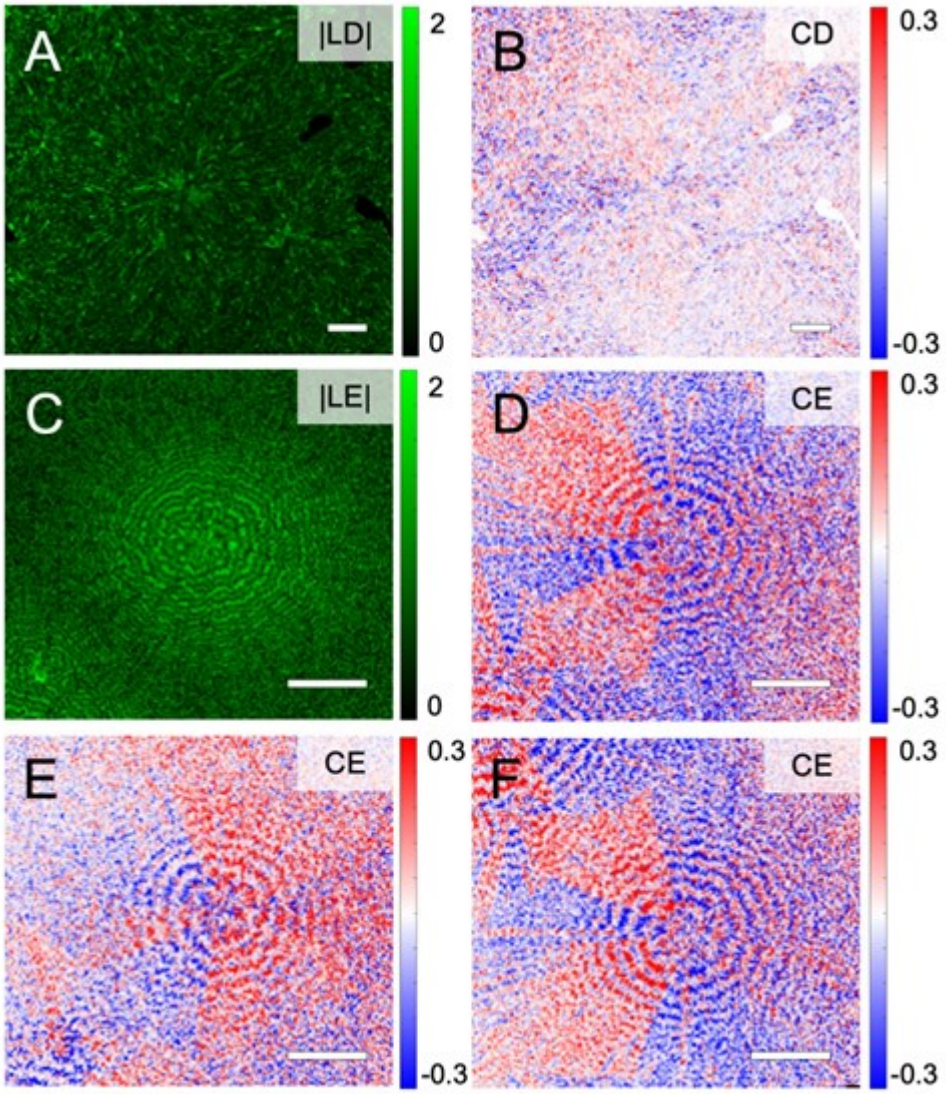

Figure 5. (A) Linear dichroism and (B) circular dichroism maps of *S* film collected at λ=540 nm. (C) Linear extinction and (D) circular extinction (CE) map of *T* films collected at λ=540 nm, respectively. CE map of *T* films collected (E) at λ=500 nm, and (F) when the film is flipped around the horizonal axis at λ=540 nm, respectively.

Organic semiconductor crystals also exhibit significant charge transport anisotropy along different crystallographic directions. Conductive atomic force microscopy (c-AFM) was carried out to measure charge transport through *S* and *T* films. A gold electrode was deposited on top of TIPS ADT films and the magnitude of current flow between the electrode and a c-AFM tip was mapped across the film surface at an applied bias of +10 V (see Figure S14 for setup diagram). Representative contact-mode height images of *S* and *T* films, (Figure 6A and B, respectively) with

the gold electrode at the top ~10 μm of the images. The surface of the *S* film exhibits a smooth morphology with a RMS roughness of 135 ± 106 nm, while that of the *T* film is rougher (383 ± 155 nm). Flat bands are separated by crevices that measure ~20 um in length, commensurate with the twisting pitch.

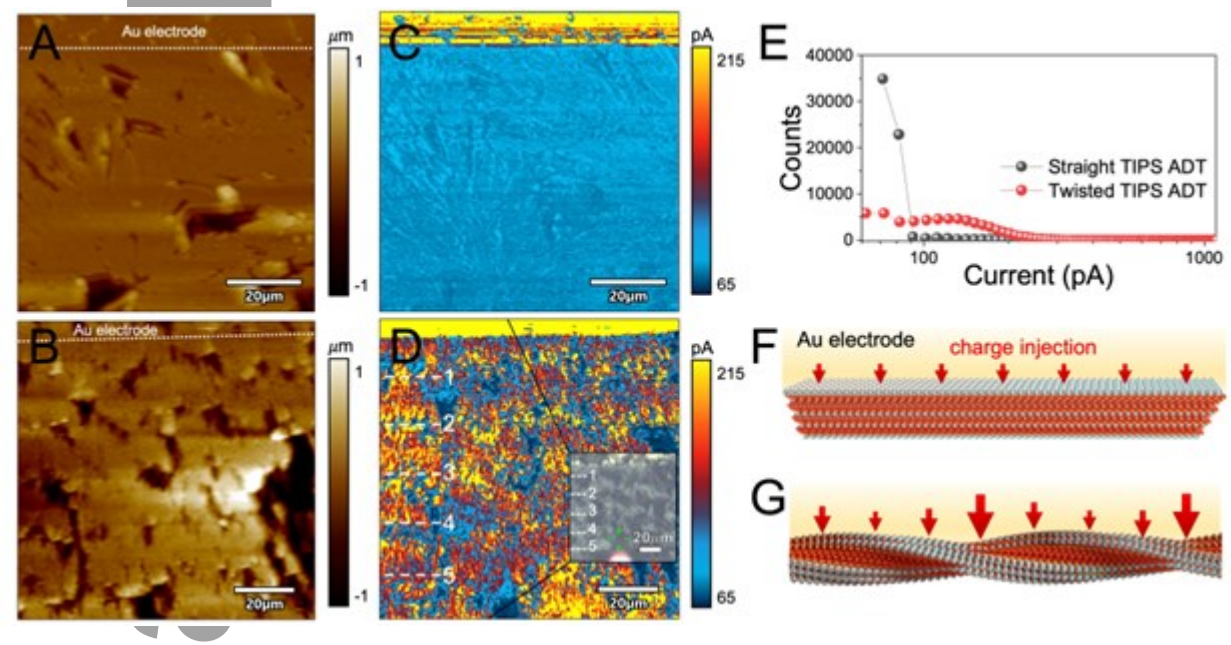

Figure 6. AFM height images (A,B) collected in contact mode and corresponding lateral current mapping images of (C, D) *S* and *T* films, respectively. Optical micrograph of the scanned region is provided as an inset in (D), with corresponding bands numbered in the c-AFM map. (E) Histograms that tabulate the counts of current level of *S* and *T* films. Schematic illustration of (F) straight and (G) twisted TIPS ADT crystals at the film/electrode interface. Red arrows qualitatively illustrate the magnitude of charge injection at different locations along the crystal.

Lateral current maps (Figure 6C, D) collected simultaneously over the regions in Figure 6A and B, respectively, at an applied bias of 10 V between the top contact gold electrode and AFM tip. The current map collected on a *S* film shows relatively uniform current levels across the 100 × 100 μm region scanned. In contrast, the current map of the *T* film showed large local, oscillatory variations in current (Figure 6D). These coarse oscillations, commensurate with the pitch, are likely related to the continually rotating orientations in *T* films. Figure 6E displays histograms of the current levels measured at each pixel in the current maps. For the *S* film, the average current was 80 ± 2 pA. For the *T* film, on the other hand, the average current was 150 ± 22 pA and the distribution of current values was much broader compared to that in the current map of the *S* film. These results are surprising considering that the *T*

film incorporates 16 wt% of insulating PE, a barrier to charge transport. There is also evidence that interconnected networks of twisted crystals can facilitate charge transport. In films of BDT crystals, for example, smaller grain boundaries exist between twisted fibrils compared to straight fibrils, leading to faster charge transport in BDT *T* films.[13]

Larger currents supported in banded spherulites may be a consequence of enhanced charge injection for specific crystal orientations. We previously found vertical charge transport through bis(triisopropylsilylethynyl)pyranthrene (TIPS PY) crystals to vary by two orders of magnitude depending on the crystal orientation. Charge transport was hindered by layers of insulating silyl groups in plane perpendicular to [001].[47] Along [100], on the other hand, charges can hop directly from one aromatic PY core to the next. *S* films adopt an orientation in which [001] is perpendicular to the substrate surface (Figure 6F). The injection or extraction of charges at the electrode or AFM tip require passage through the insulating silyl groups. In *T* films with continuously rotating orientations charge can be injected or extracted along [100], avoiding the silyl layers. In line with our findings on anisotropic charge transport through TIPS PY crystals, we expect charge injection/extraction to be significantly larger along the [100] direction compared to the [001] direction, resulting in improved current flow through *T* versus *S* films (Figure 6G).

To further assess the influence of crystal twisting on optoelectronic device performance, we fabricated photodetectors using a coplanar electrode geometry for which the active layer comprised TIPS ADT spherulites with either straight or twisted crystals, hereafter referred to as *S* and *T* photodetectors, respectively. Pure TIPS ADT and TIPS ADT mixed with 16 wt % PE were sandwiched between a glass coverslip and the device platform comprising gold electrodes thermally evaporated onto a glass slide through a shadow mask, melted at 250 ºC and crystallized as 1 μm thick films at 130 and 30 ºC, respectively. Optical micrographs of the photodetector channels (L = 30 μm, W = 220 μm) are provided as insets in Figure 7A and B.

Figure 7A and B display the current-voltage (*I-V*) curves of *S* and *T* photodetectors in the dark and under 532 nm-light irradiation with a light intensity of 2.6 mW/cm^2. The dark current levels of *S* and *T* photodetectors were 9.7 and 19 nA at the voltage of 30 V, respectively. Under 532 nm-light illumination, both *S* and *T* photodetectors exhibited photo-induced current. At an applied bias of 30 V, the photocurrent of the *T* photodetector was 170 nA, 3.3 times larger than that of the *S* photodetector. This significant improvement in *T* photodetectors is surprising considering that the active layers incorporate 16 wt % insulating PE that does not participate in photocurrent generation. Nevertheless, we can rely on an explanation that is consistent with our rationalization for the increased transport in *S* and *T* photodetectors.

Time-dependent *T* photodetectors were measured by repeatedly turning on and off light irradiation with intensities ranging from 0.2 – 2.6 mW/cm^2 in 15 s increments while measuring current flow at a fixed bias of 30 V. Consistent photocurrent was observed for both devices, as displayed in Figure 7C and D, increasing with light intensity. The photocurrent of the *T* photodetector was higher than that of the *S* photodetector for all light intensities tested. Photodetector responsivity, *R*, external quantum efficiency (EQE), and detectivity, *D*, were also characterized following equations provided in the Supporting Information.[48-50] *R* represents the generated photocurrent per unit power of the incident light on the effective area of photodetector, while the EQE is the ratio of the number of charge carriers generated per incident photon.[48] These two parameters are related by the relationship, EQE = $Rh\nu/e$, where *h* is Planck's constant, ν is the frequency of incident light, and *e* is the charge of an electron. The responsivities and EQE values of *S* and *T* photodetectors as a function of irradiance under different applied biases are presented in Figure S15 and Figure 7E and F, respectively. As observed from the graphs, the EQE values for *T* photodetectors were higher than *S* photodetectors for all light intensities tested. The highest recorded EQE values for *S* and *T* photodetectors were 292 and 606%, respectively, at an applied bias of 30 V and a light intensity of 0.2 mW/cm^2. At these conditions, *D* values, assuming limiting shot-noise, were calculated to be 1.7×10^{11} and 1.9×10^{11} Jones for *S* and *T* photodetectors, respectively (see Supporting Information for equations).

For both *S* and *T* photodetectors, the EQE values measured at 532 nm and an applied bias of 30 V were larger than 100%, indicating the generation of multiple charge carriers per incident photon. The presence of charge traps, which are prevalent in melt-processed organic semiconductor films,[13] has previously been demonstrated to improve photocurrent through a photomultiplication effect.[51] In this mechanism, photogenerated charges are trapped within the organic semiconductor layer near the electrode interface, creating an electric field that triggers tunneling charge injection from the electrode into the organic semiconductor layer.[52] One photon can generate multiple charge carriers through the tunneling current, resulting in external quantum efficiencies above 100%. The decrease in *R* and EQE with increasing light intensity is likely due to the saturation of charge traps, which results in a sublinear dependence of photocurrent on light intensity.[53]

Collectively, our results suggest that both straight and twisted TIPS ADT crystals have defects that trap photogenerated electrons, with twisted crystals exhibiting a larger trap density compared to straight crystals.[13] During light irradiation, electrons accumulate in these traps near the film-electrode interface, producing an electric field that facilitates hole tunneling through the charge injection barrier between the Au work function and the HOMO level of TIPS ADT. Such charge injection barriers are commonly observed at organic semiconductor/Au interfaces and are a

consequence of repulsion between the electrons of the organic semiconductor and metal.[54] In addition to having a higher density of traps, twisted crystals also present crystallographic orientations at the electrode interface for which charge injection is enhanced compared to other orientations, as demonstrated by c-AFM mapping. We expect that this combination of larger trap density and improved charge injection through alternating twisting bands results in significantly improved performance of *T* photodetectors compared to *S* photodetectors. Promisingly, TIPS ADT photodetectors can operate in the wavelength range of <350 – 650 nm, as displayed in wavelength-dependent EQE and *R* measurements in Figure S16. The detailed wavelength-dependent EQE setup is provided in the Experimental section. At the relatively low light intensities (μW/cm^2 range) used in this experimental setup, EQE, *R*, and *D* values as high as 5561%, 26 A/W, and 3.2 x 10^{14} Jones, respectively, were measured for *T* photodetectors. *S* photodetectors, on the other hand, exhibited maximum EQE, *R* and *D* values of only 901%, 4.1 A/W, and 5 x 10^{13} Jones, respectively. The figures of merit for *T* photodetectors are comparable to those of other organic semiconductor-based photodetectors,[49, 55] suggesting that melt-processed twisted crystal films are a viable, solvent-free strategy for emerging optoelectronic applications.

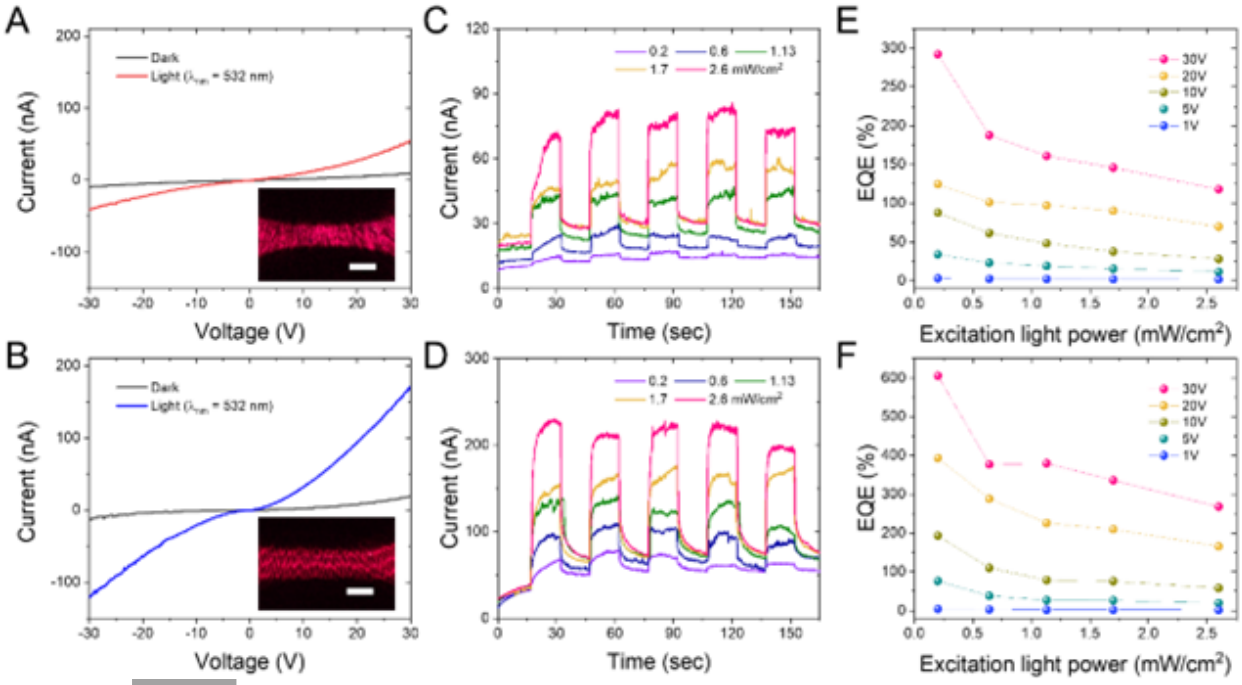

Figure 7. Current–voltage (*I–V*) curves of (A) *S* and (B) *T* photodetectors and (inset) corresponding optical micrographs (scale bar is 30 um). Time-dependent photoresponse of (C) *S* and (D) *T* photodetectors at a bias of 30 V under different irradiation power at 532 nm. EQE as a function of the illumination light excitation power (532 nm light intensity) of (E) *S* and (F) *T* photodetectors under different biases.

3. CONCLUSIONS

We examined crystal twisting as an alternative strategy to orientation control in organic semiconductor thin films. Because small-molecule organic semiconductors exhibit crystal orientation-dependent properties, crystal twisting presents a means of patterning periodicity into materials properties, including absorbance, photoluminescence, and conductivity, on the tens of microns length scale. The utility of self-patterning in this way is highlighted by the significant improvement in conductivity and photoconductivity exhibited by twisted TIPS ADT crystals compared to their straight counterparts. For straight TIPS ADT crystals, charge injection and extraction at the film/electrode interface must occur along the [001] direction where insulating triisopropylsilyl groups act as barriers for charge transport. By twisting about the growth direction, we introduce other orientations with higher conductivities along which charge injection and extraction are more efficient. For TIPS ADT and other small-molecule banded spherulites, CE arises from the twisting of crystalline fibrils irrespective of the symmetry of the molecule or crystal symmetry. Combining the circular polarization sensitivity and photoconductivity of twisted TIPS ADT semiconductor crystals may open avenues for emerging applications in circularly polarized light detection and emission.

4. EXPERIMENTAL SECTION

Materials: TIPS ADT was synthesized according to previously published procedures.[18] Medium density PE (0.94 g/mL at 25 ºC) was purchased from Sigma-Aldrich and used without further purification. To form films, 1–2 mg of TIPS ADT and TIPS ADT mixed with PE 16 wt % were placed between glass coverslips and melted on a Kofler bench at 250 ºC. The samples were then cooled and crystallized at 130 and 30 ºC, respectively.

Film Characterization: Cross-polarized optical micrographs were collected using an Olympus BX53 microscope. Grazing-incidence X-ray diffraction (GIXD) measurements were performed at Brookhaven National Laboratory on Beamline 11-BM with an incident beam energy of 13.5 keV. Scanning electron micrographs were collected with a Merlin field-emission scanning electron microscope (Carl Zeiss). Confocal fluorescence micrographs were taken with Leica TCS SP8 X laser confocal microscope with a laser excitation of 575 nm. MMI was obtained using a home-built Mueller matrix imaging polarimeter with mechanical light modulation, as described previously.[30, 41] Local absorption

and PL spectra were obtained with a microspectrophotometer (CRAIC Technologies, 508 PV). Polarized absorption spectra were acquired by mounting a broad-band wire-grid polarizer in the beam path, placed in a rotating mount, using a rotation step size of 15˚. Raman spectra were acquired using a home-built microspectroscopy setup similar to the setup described previously.[56] A tunable CW laser (Spectra physics 3900) was set at 785.54 nm (characterized by a Wavemeter) and used as the excitation source. The laser beam was cleaned by a filter (AHF analysentechnik AG, HC Laser Clean-up MaxLine 785/3), depolarized using a liquid crystal depolarizer (Thorlabs, DPP25-B). The beam was reflected by a dichroic mirror (AHF analysentechnik AG, Beamsplitter RT 785 rdc) and focused by the objective lens (Olympus Plan Achromat, 20×, NA0.4) on a sample. The laser power after the objective lens was 50 mW and the spot size was about 1 µm. The detected signal was spatially filtered by a 50 µm pinhole at the conjugate plane, and the excitation sources was cleaned by a long-pass filter (Iridian Spectral Technologies Ltd., 785 Nano Edge). Then, the Raman spectrum was recorded by a spectrograph (Andor, Kymera 193) with a CCD camera (Andor, iDus 420). Each spectrum was recorded by accumulating 10 spectra with the exposure time of 10 s.

High-Resolution X-Ray Powder Diffraction: High-resolution synchrotron PXRD data were collected at the 11-BM beamline (Advanced Photon Source at Argonne National Laboratory) using an average wavelength of 0.458955 Å. The measurements were performed at T = 100 K. Discrete detectors covering an angular range from -6 to 16 º 2θ were scanned over a 34º 2θ range, with data points collected every 0.001º 2θ and a scan speed of 0.01º/s. The final dataset included data from 0.5 to 30º 2θ. The sample was prepared by melting powder of TIPS ADT/PE mixture in 0.8 mm Kapton capillary at 280 ºC and cooling it to room temperature within seconds. To confirm the absence of preferred orientations, prior to shipping to the synchrotron, the PXRD pattern was collected in transmission mode using a Bruker D8 Discover General Area Detector Diffraction System (GADDS) equipped with a VÅNTEC-2000 2D detector and Cu-$K\alpha$ source (λ = 1.54178 Å). The X-ray beam was monochromated with a graphite crystal and collimated with a 0.5 mm capillary collimator (MONOCAP).

DFT Calculations: The initial geometry for the TIPS ADT SS packing motif was obtained from the OCELOT database (identifier com_k03230). Using the TOPAS-generated TIPS ADT crystal structure as the template, the *in silico* BW packing motif of TIPS ADT was generated using the XtalTransform tool from OCELOT infrastructure.[57] The lattice

parameters for TIPS ADT BW were constrained to the experimental XRD data. The DFT calculations were carried out with the Perdew, Burke, and Ernzerhof (PBE) exchange-correlation functional. The electron-ion interactions were described by the projector augmented-wave (PAW) method and full periodic boundary conditions using the Vienna Ab-initio Simulation Package (VASP 5.4.1).[58] A plane wave cutoff energy of 600 eV was employed. Monkhorst–Pack *k*-space sampling density of 3×3×3 was used for structure relaxation. To incorporate van der Waals' interactions, Grimme's D3 functional was used.[59] The criterion for convergence of the self-consistency cycles was 10-6 eV/atom, while the structures were relaxed until the residual cartesian force component was less than 0.02 eV $Å^{-1}$ for each atom.

Calculated band structures and absorption spectra were started from the DFT calculations carried out by the plane-wave-based Quantum ESPRESSO code.[60] Optimized norm-conserving Vanderbilt pseudopotentials[61] were used and downloaded from the PseudoDojo.[62] The PBE exchange-correlation functional[63] was employed under generalized gradient approximations (GGA). There are 4, 1, 4, and 6 valence electrons for C, H, Si, and S, respectively. 2×5×4 and 2×3×3 k-meshes were used for BW and SS TIPS ADT, respectively. An energy cutoff of 1088 eV was set for the bare Coulomb interaction. After the DFT calculations, (one-shot) GW and BSE (Bethe-Salpeter equation) were calculated by the BerkeleyGW[64] code. The energy cutoff of the screened Coulomb interaction was set to 163 eV. 814 bands were included in the dielectric function and self-energy calculations. Both DFT and GW band structures were plotted with the Wannier90 code.[65] Labels of high symmetry k-points were defined in the paper from Setyawan and Curtarolo. The Tamm-Dancoff[66] and static approximations were employed when solving the BSE. 12 valence bands and 12 conduction bands were included when calculating absorption spectra.

DFT calculations were performed with Amsterdam Modeling Suite (AMS) Driver. A single isomer of ADT was drawn on AMSinput, of which geometry was optimized using PBE-D3(BJ) function and TZP as basis set. Once the geometry was optimized, the frequencies of Raman were calculated from 0 to 3000 cm^{-1}. No factor was used to scale frequencies when comparing simulated Raman spectra with that of experiments. The *anti* isomer has a C_2 symmetry whereas the *syn* has C_S symmetry.

Conductive AFM: Conductive AFM (c-AFM) images were collected using a Jupiter XR AFM available from Asylum Research, an Oxford Company. The AFM was operated in contact mode using Ti/Ir (5/20 nm) coated AFM tips (model ASYELEC-01-R2) with spring constants between 1.4 and 5.8 N/m. Prior to measurements, top-contact Au electrodes

(50 nm) were thermally evaporated on top of TIPS ADT films through a shadow mask. Under c-AFM operation, the conductive AFM tip was placed in contact with a TIPS ADT film, and a 10 V bias was applied across the probe and a counter-electrode while the tip was scanned along the surface of the film. Current flow from the electrode to the tip was simultaneously measured along with height profiles of the film surface.

Photodetector fabrication and testing: A chromium (Cr) thin film for an adhesion layer (5 nm) and Au film for electrodes (50 nm) were thermally evaporated onto a glass coverslip through a shadow mask with a channel length of 30 μm and a channel width of 220 μm. The substrates were immersed in 1 wt % solution of PFBT (Sigma-Aldrich, 97% purity) in anhydrous ethyl alcohol (Sigma-Aldrich, 99.5% purity) in a nitrogen-filled glovebox for 30 min, then rinsed with neat ethyl alcohol and allowed to dry in the glovebox for 30 min. TIPS ADT and TIPS ADT/PE mixed powders were melted between the coverslip with electrodes and a second coverslip and cooled as described above. *I-V* curves of *S* and *T* photodetectors were characterized using a Keithley 2636B dual channel sourcemeter at room temperature. The photoresponse of both were examined using a laser with an emission wavelength of 532 nm under an optical power density from 0.2 to 2.6 mW/cm^2.

Wavelength-dependent EQE measurement[67]: Broadband light from 350 to 700 nm was generated by an incoherent 250 W Oriel Newport light source equipped with a halogen bulb. The generated light was collimated, filtered for second-order light, and optically chopped before being focused on the input slit (a Cornerstone 260 vis-NIR extended range 1/4 m monochromator). The light from the monochromator was recollimated and finally refocused onto the top of the sample placed on a stage. We measured the output powers reaching our samples using a Newport power meter at each wavelength from 350 to 700 nm with interval of 10 nm. The photovoltage generated upon exposure of TIPS ADT films to light was measured using an SR570 preampifier and SR810 lock-in amplifier connected in series. We implemented a Keithley 2400 source meter and a 1 M Ω standard resistor (Cutequeen 1/4W) to apply high bias of 30 V. The photovoltage from the lock-in amplifier were measured for 10 s at each wavelength and recorded by using a custom-developed LabView program.[67]

Supporting Information: Supporting Information is available from the Wiley Online Library.

Conflict of Interest: The authors declare no conflict of interest.

ACKNOWLEDGEMENTS

This work at New York University was primarily supported by the National Science Foundation (NSF) award number DMR-2003997 and secondarily by the New York University Materials Research Science and Engineering Center (MRSEC) program of the NSF under award number DMR-1420073. The authors also acknowledge support from PSEG to advance energy innovation at Stevens Institute of Technology. Synthetic efforts (JEA and EKH) were supported by the NSF award number DMREF-1627428. The work at the University of Kentucky was supported by the NSF award number DMR-1627428 and cooperative agreement number 1849213. Supercomputing resources were provided by the University of Kentucky Information Technology Department and Center for Computational Sciences (CCS). Use of the Advanced Photon Source at Argonne National Laboratory was supported by the U. S. Department of Energy, Office of Science, Office of Basic Energy Sciences, under Contract No. DE-AC02-06CH11357. The X-ray microdiffractometer with GADDS was acquired through the support of the NSF under award number CRIF/CHE-0840277 and NSF MRSEC Program under award number DMR-0820341. We also thank Prof. Ayaskanta Sahu and Håvard Mølnås for access to the EQE measurement setup.

References

[1] A. M. Hiszpanski, Y.-L. Loo, *Energy & Environmental Science* **2014**, 7, 592; S. H. Liu, W. C. M. Wang, A. L. Briseno, S. C. E. Mannsfeld, Z. N. Bao, *Adv Mater* **2009**, 21, 1217; X. J. Zhang, J. S. Jie, W. Deng, Q. X. Shang, J. C. Wang, H. Wang, X. F. Chen, X. H. Zhang, *Adv Mater* **2016**, 28, 2475.

[2] Y. Diao, B. C. K. Tee, G. Giri, J. Xu, D. H. Kim, H. A. Becerril, R. M. Stoltenberg, T. H. Lee, G. Xue, S. C. B. Mannsfeld, Z. Bao, *Nature Materials* **2013**, 12, 665.

[3] M. J. Han, J. Kim, B. Kim, S. M. Park, H. Ahn, T. J. Shin, B. Kim, H. Kim, D. K. Yoon, *ACS Nano* **2020**, 14, 12951.

[4] S. S. Dalal, D. M. Walters, I. Lyubimov, J. J. d. Pablo, M. D. Ediger, *Proceedings of the National Academy of Sciences* **2015**, 112, 4227.

[5] S. B. Jo, H. H. Kim, H. Lee, B. Kang, S. Lee, M. Sim, M. Kim, W. H. Lee, K. Cho, *ACS nano* **2015**, 9, 8206; Y. Zhang, Y. Diao, H. Lee, T. J. Mirabito, R. W. Johnson, E. Puodziukynaite, J. John, K. R. Carter, T. Emrick, S. C. B. Mannsfeld, A. L. Briseno, *Nano Letters* **2014**, 14, 5547; J. M. Mativetsky, H. Wang, S. S. Lee, L. Whittaker-Brooks, Y.-L. Loo, *Chemical Communications* **2014**, 50, 5319.

[6] K. Zong, Y. Ma, K. Shayan, J. Ly, E. Renjilian, C. Hu, S. Strauf, A. Briseño, S. S. Lee, *Crystal Growth & Design* **2019**, 19, 3461.

[7] A. G. Shtukenberg, Y. O. Punin, A. Gujral, B. Kahr, *Angew Chem Int Edit* **2014**, 53, 672.

[8] F. Khoury, E. Passaglia, in *Treatise on Solid State Chemistry: Volume 3 Crystalline and Noncrystalline Solids*, (Ed: N. B. Hannay), Springer US, Boston, MA 1976; B. Lotz, S. Z. D. Cheng, *Polymer* **2005**, 46, 577.

[9] A. G. Shtukenberg, X. L. Zhu, Y. F. Yang, B. Kahr, *Crystal Growth & Design* **2020**, 20, 6186.

[10] A. Shtukenberg, E. Gunn, M. Gazzano, J. Freudenthal, E. Camp, R. Sours, E. Rosseeva, B. Kahr, *Chemphyschem* **2011**, 12, 1558.

[11] Y. Yang, Y. Zhang, C. T. Hu, M. Sun, S. Jeong, S. S. Lee, A. G. Shtukenberg, B. Kahr, *Chemistry of Materials* **2022**, 34, 1778.

[12] A. G. Shtukenberg, R. Drori, E. V. Sturm, N. Vidavsky, A. Haddad, J. Zheng, L. A. Estroff, H. Weissman, S. G. Wolf, E. Shimoni, C. Li, N. Fellah, E. Efrati, B. Kahr, *Angewandte Chemie-International Edition* **2020**, 59, 14593; A. G. Shtukenberg, A. Gujral, E. Rosseeva, X. Cui, B. Kahr, *CrystEngComm* **2015**, 17, 8817.

[13] Y. F. Yang, L. S. de Moraes, C. Ruzie, G. Schweicher, Y. H. Geerts, A. R. Kennedy, H. Y. Zhou, S. Whittaker, S. S. Lee, B. Kahr, A. G. Shtukenberg, *Advanced Materials* **2022**.

[14] Y. Yang, K. Zong, S. J. Whittaker, Z. An, M. Tan, H. Zhou, A. G. Shtukenberg, B. Kahr, S. S. Lee, *Molecular Systems Design & Engineering* **2022**.

[15] A. J. Lovinger, *Macromolecules* **2020**, 53, 741.

[16] C. E. Killalea, D. B. Amabilino, *Isr J Chem* **2021**, 61, 629.

[17] H. D. Keith, F. J. Padden, *Macromolecules* **1996**, 29, 7776; S. Nagarajan, E. M. Woo, *Macromolecular Rapid Communications* **2021**, 42.

[18] M. M. Payne, S. A. Odom, S. R. Parkin, J. E. Anthony, *Organic Letters* **2004**, 6, 3325.

[19] A. Le Bail, *Powder Diffraction* **2004**, 19, 249.

[20] Bruker AXS, Karlsruhe, Germany 2017.

[21] J. E. Anthony, J. S. Brooks, D. L. Eaton, S. R. Parkin, *Journal of the American Chemical Society* **2001**, 123, 9482; J. S. Brooks, D. L. Eaton, J. E. Anthony, S. R. Parkin, J. W. Brill, Y. Sushko, *Current Applied Physics* **2001**, 1, 301.

[22] C. D. Dimitrakopoulos, A. R. Brown, A. Pomp, *J Appl Phys* **1996**, 80, 2501.

[23] K. V. Nguyen, M. M. Payne, J. E. Anthony, J. H. Lee, E. Song, B. Kang, K. Cho, W. H. Lee, *Sci Rep-Uk* **2016**, 6.

[24] H. Zhao, Z. Wang, G. Dong, L. Duan, *Physical Chemistry Chemical Physics* **2015**, 17, 6274.

[25] W. Deng, Y. L. Xiao, B. Lu, L. Zhang, Y. J. Xia, C. H. Zhu, X. J. Zhang, J. H. Guo, X. H. Zhang, J. S. Jie, *Adv Mater* **2021**, 33.

[26] J. Xu, H. Ye, S. Zhang, B. Guo, *Crystals* **2017**, 7, 241; B. Crist, J. M. Schultz, *Progress in Polymer Science* **2016**, 56, 1.

[27] P. J. Barham, A. Keller, E. L. Otun, P. A. Holmes, *Journal of Materials Science* **1984**, 19, 2781.

[28] A. Toda, K. Taguchi, M. Hikosaka, H. Kajioka, *Polymer Journal* **2008**, 40, 905.

[29] A. Keller, *J Polym Sci* **1955**, 17, 291.

[30] A. G. Shtukenberg, X. Cui, J. Freudenthal, E. Gunn, E. Camp, B. Kahr, *Journal of the American Chemical Society* **2012**, 134, 6354.

[31] A. G. Shtukenberg, Q. Zhu, D. J. Carter, L. Vogt, J. Hoja, E. Schneider, H. Song, B. Pokroy, I. Polishchuk, A. Tkatchenko, A. R. Oganov, A. L. Rohl, M. E. Tuckerman, B. Kahr, *Chemical Science* **2017**, 8, 4926.

[32] Q. Zhu, A. G. Shtukenberg, D. J. Carter, T.-Q. Yu, J. Yang, M. Chen, P. Raiteri, A. R. Oganov, B. Pokroy, I. Polishchuk, P. J. Bygrave, G. M. Day, A. L. Rohl, M. E. Tuckerman, B. Kahr, *Journal of the American Chemical Society* **2016**, 138, 4881.

[33] K. Zhao, O. Wodo, D. D. Ren, H. U. Khan, M. R. Niazi, H. L. Hu, M. Abdelsamie, R. P. Li, E. Q. Li, L. Y. Yu, B. Y. Yan, M. M. Payne, J. Smith, J. E. Anthony, T. D. Anthopoulos, S. T. Thoroddsen, B. Ganapathysubramanian, A. Amassian, *Advanced Functional Materials* **2016**, 26, 1737; T. Ohe, M. Kuribayashi, R. Yasuda, A. Tsuboi, K. Nomoto, K. Satori, M. Itabashi, J. Kasahara, *Applied Physics Letters* **2008**, 93.

[34] K. Schulze, T. Bilkay, S. Janietz, *Applied Physics Letters* **2012**, 101, 043301.

[35] A. D. Platt, J. Day, S. Subramanian, J. E. Anthony, O. Ostroverkhova, *The Journal of Physical Chemistry C* **2009**, 113, 14006.

[36] M. Grüning, A. Marini, X. Gonze, *Nano Letters* **2009**, 9, 2820.

[37] S. Sharifzadeh, *Journal of Physics: Condensed Matter* **2018**, 30, 153002.

[38] W. Woelffel, C. Claireaux, M. J. Toplis, E. Burov, E. Barthel, A. Shukla, J. Biscaras, M. H. Chopinet, E. Gouillart, *Journal of Non-Crystalline Solids* **2015**, 428, 121; O. Urquidi, J. Brazard, N. LeMessurier, L. Simine, T. B. M. Adachi, *Proceedings of the National Academy of Sciences of the United States of America* **2022**, 119.

[39] D. T. James, J. M. Frost, J. Wade, J. Nelson, J.-S. Kim, *ACS Nano* **2013**, 7, 7983.

[40] S. Sharifzadeh, C. Y. Wong, H. Wu, B. L. Cotts, L. Kronik, N. S. Ginsberg, J. B. Neaton, *Advanced Functional Materials* **2015**, 25, 2038.

[41] X. Y. Cui, S. M. Nichols, O. Arteaga, J. Freudenthal, F. Paula, A. G. Shtukenberg, B. Kahr, *Journal of the American Chemical Society* **2016**, 138, 12211.

[42] D. Gottlieb, O. Arteaga, *Opt. Express* **2021**, 29, 34723.

[43] X. Cui, A. G. Shtukenberg, J. Freudenthal, S. Nichols, B. Kahr, *Journal of the American Chemical Society* **2014**, 136, 5481.

[44] E. Gunn, R. Sours, J. B. Benedict, W. Kaminsky, B. Kahr, *Journal of the American Chemical Society* **2006**, 128, 14234.

[45] X. Cui, A. L. Rohl, A. Shtukenberg, B. Kahr, *Journal of the American Chemical Society* **2013**, 135, 3395.

[46] Y. Shindo, M. Nakagawa, *Review of Scientific Instruments* **1985**, 56, 32; Y. Shindo, M. Nakagawa, Y. Ohmi, *Applied Spectroscopy* **1985**, 39, 860; J. H. Freudenthal, E. Hollis, B. Kahr, *Chirality* **2009**, 21, E20; G. Albano, G. Pescitelli, L. Di Bari, *Chemical Reviews* **2020**, 120, 10145.

[47] X. Bai, K. Zong, J. Ly, J. S. Mehta, M. Hand, K. Molnar, S. Lee, B. Kahr, J. M. Mativetsky, A. Briseno, S. S. Lee, *Chemistry of Materials* **2017**, 29, 7571.

[48] S. Jeong, M. Choe, J.-W. Kang, M. W. Kim, W. G. Jung, Y.-C. Leem, J. Chun, B.-J. Kim, S.-J. Park, *ACS Applied Materials & Interfaces* **2014**, 6, 6170.

[49] J. L. Miao, F. J. Zhang, *Laser & Photonics Reviews* **2019**, 13.

[50] S. Dhar, T. Majumder, S. P. Mondal, *ACS Applied Materials & Interfaces* **2016**, 8, 31822; M. W. Kim, Y. H. Yuan, S. Jeong, J. Chong, H. Molnas, A. Alaei, I. Cleveland, N. Liu, Y. C. Ma, S. Strauf, E. S. Aydil, A. Sahu, D. M. Kalyon, S. S. Lee, *Advanced Functional Materials* **2022**, 32.

[51] M. Daanoune, R. Clerc, B. Flament, L. Hirsch, *Journal of Applied Physics* **2020**, 127, 055502.

[52] M. Hiramoto, T. Imahigashi, M. Yokoyama, *Applied Physics Letters* **1994**, 64, 187.

[53] C. Soci, A. Zhang, B. Xiang, S. A. Dayeh, D. P. R. Aplin, J. Park, X. Y. Bao, Y. H. Lo, D. Wang, *Nano Letters* **2007**, 7, 1003.

[54] N. Koch, A. Kahn, J. Ghijsen, J.-J. Pireaux, J. Schwartz, R. L. Johnson, A. Elschner, *Applied Physics Letters* **2003**, 82, 70; P. Marmont, N. Battaglini, P. Lang, G. Horowitz, J. Hwang, A. Kahn, C. Amato, P. Calas, *Organic Electronics* **2008**, 9, 419.

[55] X. Zhao, T. Liu, H. Liu, S. Wang, X. Li, Y. Zhang, X. Hou, Z. Liu, W. Shi, T. J. S. Dennis, *ACS Applied Materials & Interfaces* **2018**, 10, 42715.

[56] C.-W. Huang, X. You, P. J. Diemer, A. J. Petty, J. E. Anthony, O. D. Jurchescu, J. M. Atkin, *Communications Chemistry* **2019**, 2, 22.

[57] Q. Ai, V. Bhat, S. M. Ryno, K. Jarolimek, P. Sornberger, A. Smith, M. M. Haley, J. E. Anthony, C. Risko, *The Journal of Chemical Physics* **2021**, 154, 174705; V. Bhat, C. Risko, 2021.

[58] G. Kresse, J. Hafner, *Physical Review B* **1993**, 47, 558; G. Kresse, J. Furthmüller, *Computational Materials Science* **1996**, 6, 15; G. Kresse, D. Joubert, *Physical Review B* **1999**, 59, 1758.

[59] S. Grimme, J. Antony, S. Ehrlich, H. Krieg, *Journal of Chemical Physics* **2010**.

[60] P. Giannozzi, S. Baroni, N. Bonini, M. Calandra, R. Car, C. Cavazzoni, D. Ceresoli, G. L. Chiarotti, M. Cococcioni, I. Dabo, A. Dal Corso, S. de Gironcoli, S. Fabris, G. Fratesi, R. Gebauer, U. Gerstmann, C. Gougoussis, A. Kokalj, M. Lazzeri, L. Martin-Samos, N. Marzari, F. Mauri, R. Mazzarello, S. Paolini, A. Pasquarello, L. Paulatto, C. Sbraccia, S. Scandolo, G. Sclauzero, A. P. Seitsonen, A. Smogunov, P. Umari, R. M. Wentzcovitch, *Journal of Physics: Condensed Matter* **2009**, 21, 395502; P. Giannozzi, O. Andreussi, T. Brumme, O. Bunau, M. Buongiorno Nardelli, M. Calandra, R. Car, C. Cavazzoni, D. Ceresoli, M. Cococcioni, N. Colonna, I. Carnimeo, A. Dal Corso, S. de Gironcoli, P. Delugas, R. A. DiStasio, A. Ferretti, A. Floris, G. Fratesi, G. Fugallo, R. Gebauer, U. Gerstmann, F. Giustino, T. Gorni, J. Jia, M. Kawamura, H. Y. Ko, A. Kokalj, E. Küçükbenli, M. Lazzeri, M. Marsili, N. Marzari, F. Mauri, N. L. Nguyen, H. V. Nguyen, A. Otero-de-la-Roza, L. Paulatto, S. Poncé, D. Rocca, R. Sabatini, B. Santra, M. Schlipf, A. P. Seitsonen, A. Smogunov, I. Timrov, T. Thonhauser, P. Umari, N. Vast, X. Wu, S. Baroni, *Journal of Physics: Condensed Matter* **2017**, 29, 465901.

[61] D. R. Hamann, *Physical Review B* **2013**, 88, 085117.

[62] M. J. van Setten, M. Giantomassi, E. Bousquet, M. J. Verstraete, D. R. Hamann, X. Gonze, G. M. Rignanese, *Computer Physics Communications* **2018**, 226, 39.

[63] J. P. Perdew, K. Burke, M. Ernzerhof, *Physical Review Letters* **1996**, 77, 3865.

[64] M. S. Hybertsen, S. G. Louie, *Phys Rev B Condens Matter* **1986**, 34, 5390; M. Rohlfing, S. G. Louie, *Physical Review B* **2000**, 62, 4927; J. Deslippe, G. Samsonidze, D. A. Strubbe, M. Jain, M. L. Cohen, S. G. Louie, *Computer Physics Communications* **2012**, 183, 1269.

[65] G. Pizzi, V. Vitale, R. Arita, S. Blügel, F. Freimuth, G. Géranton, M. Gibertini, D. Gresch, C. Johnson, T. Koretsune, J. Ibañez-Azpiroz, H. Lee, J.-M. Lihm, D. Marchand, A. Marrazzo, Y. Mokrousov, J. I. Mustafa, Y. Nohara, Y. Nomura, L. Paulatto, S. Poncé, T. Ponweiser, J. Qiao, F. Thöle, S. S. Tsirkin, M. Wierzbowska, N. Marzari, D. Vanderbilt, I. Souza, A. A. Mostofi, J. R. Yates, *Journal of Physics: Condensed Matter* **2020**, 32, 165902.

[66] S. M. Dancoff, *Physical Review* **1950**, 78, 382.

[67] M. R. Scimeca, N. Mattu, I. J. Paredes, M. N. Tran, S. J. Paul, E. S. Aydil, A. Sahu, *The Journal of Physical Chemistry C* **2021**, 125, 17556.

A generalizable strategy for introducing periodic variations in the out-of-plane orientations of 5,11-bis(triisopropylsilylethynyl)anthradithiophene (TIPS ADT) crystals via twisting is presented. Films comprising twisted TIPS ADT crystals exhibit enhanced charge injection/extraction and photoconductivity compared to those comprising straight TIPS ADT crystals because twisted TIPS ADT crystals possess out-of-plane orientations that present smaller barriers to charge injection and extraction.

Sehee Jeong, Natercia Barbosa, Akash Tiwari, Emma K. Holland, Ling-Yi Huang, Vinayak Bhat, Yongfan Yang, Yuze Zhang, St. John Whittaker, Min-Woo Kim, Aida Alaei, Pallavi Sundaram, Rochelle Spencer, Johanna Brazard, Dilhan Kalyon, Chad Risko, John E. Anthony, Takuji B. M. Adachi, Alexander G. Shtukenberg, Bart Kahr, and Stephanie S. Lee*

Twisted Crystalline Organic Semiconductor Photodetectors